PNAS PERSPECTIVE

Growing three-dimensional objects with light

Gabriel Lipkowitz[a,1], Max A. Saccone[b,c,1], Matthew A. Panzer[d], Ian A. Coates[b], Kaiwen Hsiao[b,c], Daniel Ilyn[a], Jason M. Kronenfeld[e], John R. Tumbleston[d], Eric S. G. Shaqfeh[a,b], and Joseph M. DeSimone[b,c,2]

Edited by Frank Bates, University of Minnesota Twin Cities, Minneapolis, Minnesota; received August 8, 2023; accepted March 7, 2024

Vat photopolymerization (VP) additive manufacturing enables fabrication of complex 3D objects by using light to selectively cure a liquid resin. Developed in the 1980s, this technique initially had few practical applications due to limitations in print speed and final part material properties. In the four decades since the inception of VP, the field has matured substantially due to simultaneous advances in light delivery, interface design, and materials chemistry. Today, VP materials are used in a variety of practical applications and are produced at industrial scale. In this perspective, we trace the developments that enabled this printing revolution by focusing on the enabling themes of light, interfaces, and materials. We focus on these fundamentals as they relate to continuous liquid interface production (CLIP), but provide context for the broader VP field. We identify the fundamental physics of the printing process and the key breakthroughs that have enabled faster and higher-resolution printing, as well as production of better materials. We show examples of how in situ print process monitoring methods such as optical coherence tomography can drastically improve our understanding of the print process. Finally, we highlight areas of recent development such as multimaterial printing and inorganic material printing that represent the next frontiers in VP methods.

3D printing | additive manufacturing | computational fabrication

Additive manufacturing (AM), also known as 3D printing, is a family of processes that enable rapid fabrication of complex computer-aided design (CAD) models. Three-dimensional models, created by CAD or topology optimization algorithms, are "sliced" into layers, and then deposited sequentially or "additively." Compared to subtractive methods, which remove material from a solid to shape a part, and formative methods, which use molds to define part shape, AM is well suited to rapid prototyping and the fabrication of complex geometries. This perspective focuses on vat photopolymerization (VP) techniques, which use light-initiated polymerization to selectively polymerize or "cure" a monomeric/oligomeric photoresin (1). VP methods have emerged as an indispensable part of the AM ecosystem due to their ability to form polymeric parts with high resolution and good surface finish, at high speed using relatively inexpensive instrumentation that has allowed more users to take advantage of digital fabrication. Despite their promise, VP methods still have opportunities for improvement in speed, resolution, and attainable material properties. Through the lens of light, materials, and interfaces, this perspective highlights the key developments in the VP field and identifies areas where further research, development, and understanding are needed. We focus on these fundamentals in continuous liquid interface production (CLIP), while providing context for the rest of the VP field.

VP in Context. Many different strategies enable additive part fabrication; some of the most common are material extrusion, binder jetting, powder bed fusion, and VP. Material extrusion shapes a part by extruding material from a motion-controlled nozzle. A key criterion of extrusion methodologies is that the printed material must be able to pass through the nozzle during printing, but also must remain stable and self-supporting once extruded. For example, fused deposition modeling deposits heated thermoplastic filaments, and direct ink writing (2) deposits shear-thinning and thixotropic inks which flow due to the high shear stress during extrusion through a nozzle, but recover their structural integrity quickly and do not flow after the inks are extruded. Binder jetting techniques use a liquid binder to selectively bind precursor powders together, followed by thermal treatment to fuse the powder precursors and remove the binder (3). Powder bed fusion techniques melt or sinter precursor powders to define part shape (4).

VP approaches display distinct advantages and limitations when compared to other AM techniques. Compared with other printing methods, the reduced anisotropy and

Author affiliations: [a]Department of Mechanical Engineering, Stanford University, Stanford, CA 94305; [b]Department of Chemical Engineering, Stanford University, Stanford, CA 94305; [c]Department of Radiology, Stanford University, Stanford, CA 94305; [d]Carbon, Inc., Redwood City, CA 94063; and [e]Department of Chemistry, Stanford University, Stanford, CA 94305

Author contributions: M.A.P. performed research; G.L., M.A.S., M.A.P., I.A.C., K.H., D.I., J.M.K., J.R.T., E.S.G.S., and J.M.D. wrote the paper.

Competing interest statement: J.M.D. declares that he has an equity stake in Carbon Inc. and M.A.P. and J.R.T. declare that they are employees of Carbon, Inc., which is a venture-backed start-up company that owns related U.S. Patent 9,040,090, U.S. Patent 9,216,546, U.S. Patent 9,360,757, and others. M.A.S. advises 3D Architech, a VP-based metal 3D printing company. J.M.D., M.A.P., and J.R.T. declare that they have an equity stake in Carbon, Inc. due to current or previous employment at Carbon Inc. J.M.D. declares that he is an inventor on related U.S. Patent 9,040,090, U.S. Patent 9,216,546, U.S. Patent 9,360,757, and others. G.L., I.A.C., and J.M.D. declare that they are named co-inventors in methods for multimaterial iCLIP and related pending patent applications. J.M.D. declares that his lab at Stanford is sponsored by the Wellcome Leap Foundation and the Bill and Melinda Gates Foundation. J.M.D. declares, that as a co-founder, board member, and former CEO, and as an active researcher in additive manufacturing, that he has had hundreds of social media and journalist interviews about Carbon and additive manufacturing.

This article is a PNAS Direct Submission.

[1]G.L. and M.A.S. contributed equally to this work.

[2]To whom correspondence may be addressed. Email: jmdesimone@stanford.edu.

This article contains supporting information online at https://www.pnas.org/lookup/suppl/doi:10.1073/pnas.2303648121/-/DCSupplemental.

Published July 1, 2024.

exceptional resolution of VP, with resolution specifications in typical commercially available systems on the order of tens of microns, opens the opportunity to design products with a wide range of geometries. These include the design of architected metamaterials (5), elastic microstructures (6), and Voronoi foams (7), with applications including energy-absorbing or energy-returning structures (8), soft robotics (9), and biomedical devices (10).

In order for the field to continue to innovate and foster the translation of VP materials into useful applications, it is critically important to return to the fundamentals of light, materials, and curing interfaces. For each of these three sections, we will provide a brief overview of the mechanisms that govern a key aspect of the VP process, and show how these fundamentals have been leveraged to create breakthroughs.

Advances in Photopatterning

VP techniques use light to shape polymeric parts through selective curing of a polymer resin. In the following sections, we discuss how volumetric pixel or "voxel" patterning approaches affect speed and scalability, and the development of light delivery techniques that have enabled modern printing processes. Finally, we will discuss the basics of photoresin chemistry for VP printing and a framework for controlling light propagation in photoresins.

Geometric Considerations. VP strategies are notable for their wide variety of possible printer configurations. Scanning stereolithography techniques (colloquially "SLA printing," deriving from the term "stereolithography") create a voxel by focusing an ultraviolet (UV) laser to a spot which is raster scanned to cure a single layer of resin, shown schematically in Fig. 1*A*. Photoinitiation can also be carried out with absorption of two or more (usually infrared) photons in a process known as two-photon lithography (TPL) or multiphoton lithography (MPL), which functionally operates similarly to scanning stereolithography, but with much smaller voxel sizes that can be focused throughout the photoresin Fig. 1*B*. TPL/MPL enables fabrication of structures with feature sizes below the diffraction limit of light (11), and has been demonstrated for features as small as 65 nm (12), and as small as 9 nm when combined with a second inhibition laser (13). Because only a single voxel is exposed at a time, scanning stereolithography techniques can have laser spots with high intensity, but also require large translational speeds to achieve high throughput.

In contrast, projection stereolithography techniques (colloquially digital light processing or "DLP") cure an entire layer of resin at once by projecting a two-dimensional image into the photoresin vat, shown schematically in Fig. 1*C*. This is achieved by using either a digital micromirror device (DMD) or a liquid crystal display (LCD) as a dynamic mask for a UV source. Projection stereolithography systems expose many voxels simultaneously; for example, a typical DMD has 2,560 × 1,600 pixels, allowing a DMD-based projector to simultaneously address over 4 million voxels. Compared to SLA techniques, projection techniques tend to expose each voxel with a lower intensity, but for a longer duration. CLIP is a variation of DLP printing that uses oxygen to inhibit polymerization at the interface between the photoresin and the oxygen-permeable window, forming a dead zone that facilitates resin reflow in the vat and rapid printing (15) (Fig. 1*D*). Other variations of DLP printing include the use of dual-wavelength printing, in which one wavelength initiates polymerization and a second wavelength inhibits polymerization, which, due to the ability to tune inhibition volumes, can also effect single-exposure topographical patterning (16).

Finally, volumetric additive manufacturing (VAM) techniques create a three-dimensional light intensity distribution to cure parts within a volume of liquid photoresin. For example, computed axial lithography (14) and tomographic AM (17) achieve tomographic reconstruction by superimposing images projected from different angles into a rotating vat of photocurable resin, allowing entire parts to be cured within seconds (Fig. 1*E*). The effect of simultaneous curing in VAM is achieved due to a nonlinear curing response to light dose resulting from the existence of a gelation threshold for the resin.

In 2020, a dual-wavelength VAM technique known as xolography was reported, in which a light sheet at one wavelength activates a dual color photoinitiator from a dormant state to a latent state, and an orthogonal projected image of light at a second wavelength activates the latent photoinitiator to initiate polymerization (18). Xolography,

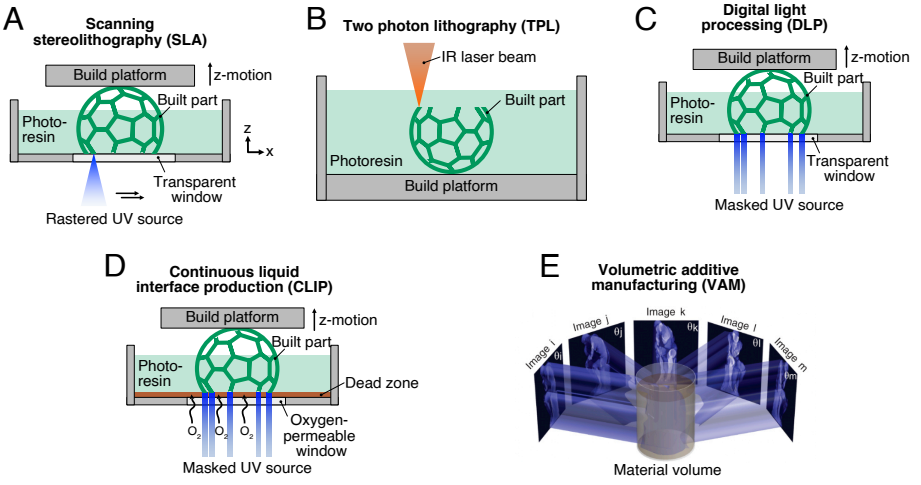

Fig. 1. Schematic of AM methods. Schematics of common VP techniques including (*A*) scanning stereolithography, (*B*) two photon lithography, (*C*) digital light projection, (*D*) continuous liquid interface production, and (*E*) volumetric AM, specifically computed axial lithography, adapted with permission from ref. 14. Support structures may be needed for some techniques but are omitted for clarity.

therefore, prints objects in a layer-by-layer fashion, but the layers are defined by the light sheet rather than physical interfaces. Volumetric stereolithography techniques can fabricate entire objects in seconds, enabling the use of viscous resins due to the lack of mass transport limitations, and enable overprinting or encapsulation of existing objects.

In the next section, we trace the development of light delivery techniques that have enabled faster and more precise VP printing.

Light Delivery Techniques. The first 3D printing techniques used a raster scanned point source (optical fiber or cathode ray tube) or masked projection to form three-dimensional objects. These techniques were notably slow and were limited by the conceptualization of masks as physical objects that had to be changed for every new cross-sectional design.

In 1981, Hideo Kodama filed the first patent for a VP technology (19), which used masked projection to introduce a 2D image to a vat of resin (Fig. 2*A*). The masks utilized in this system consisted of "black ink on transparent films" that were each individually hand-drawn or composed using a computer-controlled x-y plotter. Soon thereafter, Charles Hull introduced the term "stereolithography" in a 1984 patent, deemed "the application of lithographic techniques to production on three-dimensional objects" (20) shown schematically in Fig. 2*B*. Similarly, in Hull's conception, masks were static physical objects. Hull noted that "whenever that cross-sectional shape is to be changed, a new mask for that particular cross-sectional shape must be substituted and properly aligned."

Subsequent breakthroughs in light delivery replaced physical masks with displays that dynamically masked a light source, obviating the need for a series of physical masks to form a three-dimensionally complex part. In 1997, Bertsch et al. used an LCD to mask light from a visible laser to project 2D patterns of light, coined "microstereophotolithography" (21). In 2005, Sun et al. built on the idea of dynamic masks by substituting a DMD for the LCD to control 2D light patterning, enabling higher contrast, faster switching speeds, and smaller pixel sizes in a technique they called "projection microstereolithography" (PμSL) (22). Today, both LCDs and DMDs are commonly used as dynamic masks in projection-based VP.

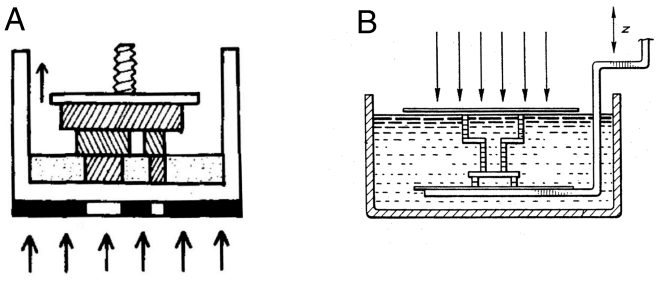

Fig. 2. Schematics from Kodama's and Hull's pioneering works. (*A*) Schematic from Kodama's 1981 work depicting bottom–up projection of 2D image into resin vat. Adapted with permission from ref. 19. Copyright 1981 American Institute of Physics. (*B*) Schematic from Hull's 1984 patent, in which photopatterning is controlled by a masked and collimated UV light source. Adapted from ref. 20.

Next, we show how chemistry developed in the early 20th century was adapted into photoresin chemistry for 3D printing through key advances in process understanding.

Photoresin Chemistry. VP 3D printing processes rely on liquid photoresins that polymerize and solidify when exposed to light. How and why that polymerization takes place has direct implications for print speed, precision, and the mechanical properties of printed parts.

While many photcurable resin chemistries exist (discussed further in the *Photopolymer Advances* section) most VP techniques make use of photoinitiated radical polymerization to shape parts by solidifying resin only where light exposure occurs (Fig. 3). Radical polymerization is inhibited by the formation of stable peroxy radicals in the presence of oxygen, quenching initiation and radical propagation (23). Such oxygen inhibition is critical to VP techniques such as CLIP (15) and likely plays a role in other SLA and DLP techniques that make use of oxygen-permeable interfaces such as polydimethyl siloxane (PDMS) or Teflon. During photoinitiation, the absorption of an appropriately energetic incident photon by a photoinitiator generates radicals, which then lead to radical polymerization. Photoinitiation chemistry dates back to 1937, when Norrish and Bamford reported the photodecomposition of aldehydes and ketones (24); photoinitiation processes are commonly referred to as Norrish Type I if an initiator undergoes homolytic bond cleavage to form radicals, or Norrish Type II if a sensitizer and coinitiator work together to form a radical species.

Today, the majority of common photoinitiators are small molecules such as acyl phosphine oxides, which absorb well in the near-UV (370 to 400 nm) (25). A wider range of photoinitiators exist that absorb at wavelengths from the mid-UV to near-IR (245 to 850 nm) (26), but commercial systems mainly use near-UV to deep blue (365 to 405 nm) light sources due to their compatibility with Type I initiators which are typically restricted to wavelengths <420 nm (27) but yield rapid curing (<10 s per layer) at reasonable light intensities (<10 mW/cm^2), which is important for commercial systems. In contrast, visible photoinitiators tend to rely on use of a photoredox catalyst,

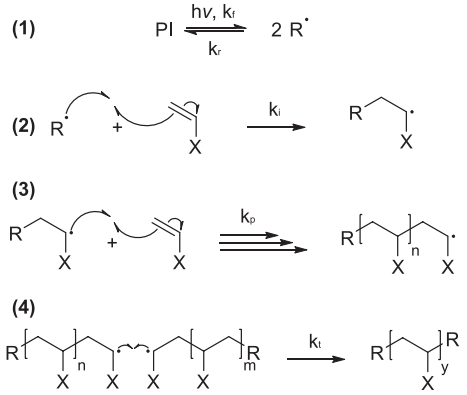

Fig. 3. Scheme of photoinitiated radical chain-growth polymerization. 1) A photoinitiator (PI) is homolytically cleaved to form radicals. 2) Initiation of polymerization by a radical. 3) Propagation of a radical across a double bond leading to polymerization. 4) Termination due to combination of two propagating chains.

which usually results in slow curing (>60 s per layer) and requires higher intensities (>20 mW/cm^2) due to a multistep reaction mechanism; in 2020, Ahn et al. reported rapid photopolymerization with visible photoinitiators (27), pointing to these systems as a promising possibility for the future of the field. Other novel initiators include polymeric photoinitiators with high molecular weight and low diffusivity (28), which can reduce postcure migration of unreacted initiators.

Acrylate-based reactive monomer systems are common in projection stereolithography platforms and are well studied (29). These systems generally gel via radical polymerization, which can exhibit complexity in propagation, chain transfer, and termination mechanisms. Intramolecular radical transfer via a secondary propagating radical is the primary mechanism desired for 3D printing, but tertiary mid-chain radicals may also form with further intramolecular migration, hydrogen shifts, branching, and β-scission possible (30). Photoinitiation and polymerization kinetics have a direct impact on cured part properties. For example, photoinitiation rate (related to both photoinitiator concentration and incident light intensity) can modulate the kinetic chain length (31), the number of monomer units consumed per initiator radical. Variations in chain length and crosslink density in turn can tune properties such as glass transition temperature (32) and modulus of the cured polymer (33).

Controlling Light Propagation in Resins. To achieve high-resolution prints, it is critical to spatially localize polymerization. Unmitigated light propagation in resin media can lead to "overcure," the undesired curing of resin beyond the intended curing area. The ability for a resin to attenuate light can be characterized with the Jacobs working curve (34), which assumes Beer–Lambert absorbance of the resin, expressed as $E = E_0 e^{(-z/D_p)}$, where E_0 is the UV dose at $z = 0$ (at the polymerization interface), z is the height above polymerization interface, and D_p is "penetration depth," the characteristic length scale for exponential decay of UV dose in resin. This analysis also assumes that after absorbing a certain dose of UV light, known as the critical cure dose E_c, a liquid photoresin will gel due to the resulting polymer no longer being soluble in the monomer resin. When exposing a liquid resin to a beam of light, this is expressed as $E(z = C_d) = E_c$. Together, this gives the working curve equation $C_d = D_p \ln(E_0 / E_c)$. Experimentally, plotting measured film thickness C_d vs. the natural logarithm of the exposure dose E_0 allows one to easily find D_p and E_c as the slope and intercept of the resulting plot. Since Jacobs' introduction of the working curve concept, the basic assumptions have largely remained the same, but some variations regarding the implementation and nomenclature have arisen for situations with suspended particles that scatter light (35), or for considering a volumetric dose (36). The working curve characterization approach has been used to model and correct for overcure due to repeated light exposures during printing, enabling fine-tuning printing parameters (36–38). This framework also intuitively shows how resin modification can improve resolution. For example, the penetration depth of resins can be reduced by adding UV absorbing agents (39, 40) or by mechanically blocking UV light from penetrating into the printed object (41).

Accelerating Printing through Advances in Interfaces

3D printing processes must be fast in order to be adopted in real-world manufacturing. A summary of the throughput of state-of-the-art methods is shown in Table 1, contextualized with their respective resolutions. The time required for photopatterning discussed in the previous section is only one of many factors that contribute to the overall speed of VP processes. Fig. 4 summarizes these for CLIP: a) light exposure duration, b) platform velocity, c) layer thickness, and d) delay time between layers. Similar factors fundamentally determine the speed of various VP techniques, but the exact kinematics vary by printing process as explained below.

Managing Part-Window Adhesion in SLA and DLP. In traditional SLA and DLP printing, objects adhere to the window during curing and must be forcibly detached. Separation forces exert significant stresses on each layer of the growing object, which have been studied in detail via computational modeling (50), online force monitoring (51, 52), and through the use of deep learning predictions (53). If separation forces are greater than the work of adhesion between the part's initial layer and the build platform, or any surface users employ to overprint on existing objects (54), adhesive failure between the growing part and the platform occurs. Separation forces can also cause delamination of subsequent layers and newly cured layers, i.e., cohesive failure. In either case, significant time and material is wasted. Even if parts remain attached to the platform, such suction forces can cause significant print defects, e.g., observable layering and stair-stepping (55). These forces scale with the size of the part and the printing speed, limiting both.

Traditional SLA and DLP printers utilize a lift-and-retract mechanism whereby the object is forcibly detached every layer. Various approaches have been attempted to alleviate separation forces to accelerate printing, including sliding mechanisms, vibration-assisted methods (56), with induced resin reflow via programmed tilt (57), with variable tensioning film systems (58), and hydraulically assisted active separation methods (59). Regardless of the mechanism, the need to address separation forces slows down printing significantly.

Table 1. Resolution-throughput in VP methods

Printing method	Linear speed*	Voxel throughput*	Resolution*	Reference
CLIP	17 mm/min	150 mm^3/s	4.5 μm	(15, 42)
HARP	7 mm/min	280 mm^3/s	100 μm	(43)
TPP	1,000 mm/s	8.7 mm^3/h	175 nm	(44, 45)
Holographic	n/a	10^6 mm^3/h	100 μm	(46)
VAM	n/a	800 mm^3/s	300 μm	(47)
Xolographic	10 mm/min	55 mm^3/s	50 μm	(18)
PμSL	6 mm/min	215 mm^3/min	0.6 μm	(22, 48)

*Best-case metrics are reported for all methods for the provided references.

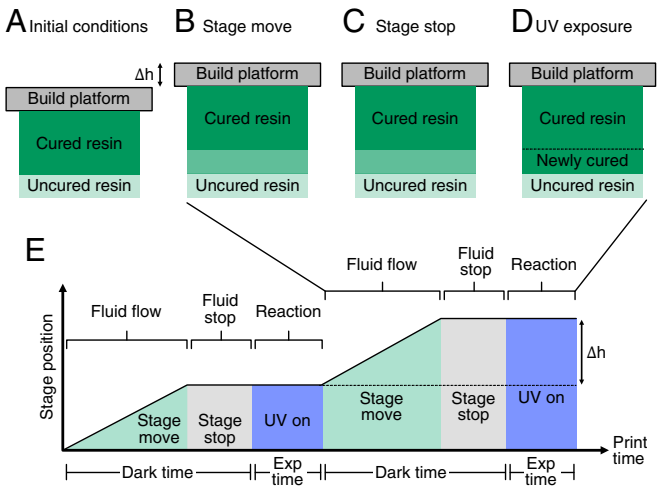

Fig. 4. Factors that affect CLIP speed specifically include chemical kinetics, fluid dynamics, and supporting machine movement. (*A*) Initially, the build platform is stationary and uncured resin is quiescent. (*B*) The stage moves a layer thickness Δh. (*C*) After moving the prescribed layer height, the stage stops, and the resin settles. (*D*) Once the resin is again quiescent, UV exposure cures a new layer of resin. (*E*) Coordinated stage movement and UV exposure as a function of time. Adapted from ref. 50.

Reducing Adhesion Forces with CLIP. Applying the well-known role of oxygen as a free radial photopolymerization inhibitor (60) to VP, in 2015 Tumbleston et al. reported CLIP printing, using an oxygen-rich "dead zone" to prevent resin from curing onto the window (Fig. 5). By obviating the lift-and-retract mechanism of SLA and DLP, this accelerated printing by up to orders of magnitude, depending on part geometry (15). Moreover, the lack of a need to forcibly separate the object from the window allowed for layerless objects with unprecedentedly smooth surface finish and isotropic mechanical properties (61). CLIP's dead zone required the build window to be highly oxygen permeable. Windows for SLA and DLP such as PDMS are oxygen-permeable to facilitate part-window detachment and can be enhanced with air-diffusion-channels (62, 63) and other surface modifications (64). However, PDMS can cloud due to solvent absorption over time, and has lower oxygen permeability than Teflon AF, which was initially used for CLIP. Teflon has an oxygen permeability of 1,000 barrers, resulting in dead zone thickness ranging from 20 μm to 100 μm that could be enhanced with concentrated oxygen (15), enabling printing at speeds of meters per hour.

Nonetheless, limitations on process speed remained, largely due to mass transport limitations on resin flow through the thin dead zone, and the introduction of Stefan adhesion forces that scale dramatically with part size. From lubrication theory, for a cylindrical part of radius R:

$$F_{Stefan} = \frac{-3\pi R^4 \mu U}{h^3}$$

where μ is dynamic resin viscosity, U is print speed, h is dead zone thickness, and R is part radius. This force can cause part delamination or cohesive failure. If drawn too fast, the build window can flex or "drum" (65–67). Large negative pressures in the dead zone can also cause resin degassing or cavitation, leading to part deformation. These forces limit print sizes, necessitate cumbersome supporting scaffolds as in traditional VP techniques, and impose a printing "speed limit."

Various strategies have been developed to further accelerate CLIP. To prevent window drumming, rigid composite build windows have been investigated, combining a rigid supporting substrate with a semipermeable membrane. More advanced mechatronic control mechanisms have been developed as well. CLIP-based printers, while initially introduced with a fully continuous stage motion mechanism, may also operate under stepped motions, interspersing UV exposure with incremental upward stage movements or pumped motions to facilitate resin reflow. Recently, we have shown that microfluidic injection into the dead zone can alleviate deleterious suction forces (42).

Addressing Thermal Limitations. In addition to interface forces, another limitation on print speed is the exothermicity of the photopolymerization reaction. If uncontrolled, this can cause runaway polymerization and damage window hardware. In 2019, Walker et al. reported a "high area rapid printing" (HARP) technique, which made use of a fluorinated oil liquid interface for printing, enabling heat dissipation during rapid prints (43). Fig. 6 shows how this strategy can reduce the accumulated heat during several printing conditions.

Visualizing Printing in Real-Time with OCT. In situ observation of the printing process can elucidate the role of the printing interface in improving print speed, and also identify print interface limitations. Optical coherence tomography (OCT) is a broad-band interferometric microscopy technique that is capable of noninvasive in situ imaging of the print process with micron-scale resolution with subsecond frame rates (68, 69). While the use of OCT is well established in many biological fields (70–74), its use as a metrology tool in AM is relatively new. Here, we demonstrate how OCT can provide a means to directly visualize and measure the range of phenomena that occur during the vat polymerization

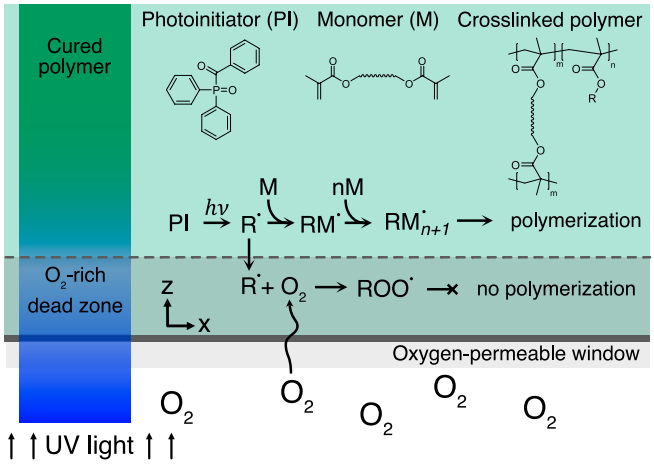

Fig. 5. Photoinduced free radical polymerization with acrylate monomers and oxygen inhibition. Interaction of UV light with a photoinitiator generates radicals that initiate free radical photopolymerization to define the shape of a 3D printed part. In acrylate-based resins, dissolved oxygen in the resin must be consumed before gelation can occur. In CLIP (pictured) additional oxygen is delivered to a thin region near the window known as the dead zone, preventing resin from curing on the window.

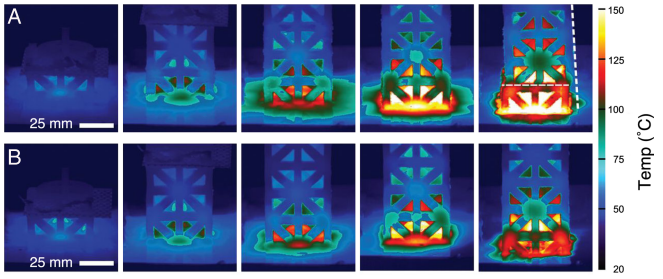

Fig. 6. Thermal control with a mobile interface. Infrared camera images of prints (*A*) without a mobile interface and (*B*) with a mobile interface show a reduction in accumulated heat during printing when incorporating a mobile interface that can convectively remove heat. Figure adapted with permission from ref. 43.

process including cure front development, window interface dynamics, and flow fields.

Fig. 7*A* shows schematically the use of an OCT microscope for real-time, noninvasive imaging of print dynamics. OCT enables direct observation of phenomena such as an oxygen-inhibition zone, observable as a darker region between the bottom of the part and the window in Fig. 7*B*, and window-drumming. OCT images can enable measurement of the complex flow field in the build zone, revealing the shape of the flow field inside the dead zone and the presence of stagnation points at the center line (Fig. 7*B*), which qualitatively agree with our analytical modeling of flow in the dead zone (Fig. 7*C*) (42).

OCT can also be used to better understand printing interfaces and accelerate the evolution of VP technologies. Fig. 8 provides an example using OCT imaging to capture some of the differing and complex phenomena that can occur with immiscible liquid-based windows, which are at the opposite extreme of window compliance compared to the rigid window case shown in Fig. 7*B*. Fig. 8 shows a snapshot during the print in "pumped" (reciprocating mode) of a 2 mm diameter cylinder in a liquid resin (the region seeded with particles) floating on top of a Krytox GPL101 immiscible liquid layer (the darker region without particles). This is similar to HARP interfaces (43), but with no transverse flow imposed on the Fluorinert in this example. The OCT imaging (Fig. 8*A*) reveals that when the Fluorinert immiscible liquid is not degassed prior to use, a dead zone is present and visible between the end of the curing part and the immiscible liquid due to the large solubility of oxygen in fluorinated liquids (75). When the Fluorinert is degassed prior to use (Fig. 8*B*) that dead zone is significantly reduced, consistent with the behavior of the deoxygenated dead zone (15). Full videos of both processes under the aforementioned varying conditions are provided in *SI Appendix*. Such insights provided by OCT imaging can be critical in understanding and optimizing resin reflow into the build zone at these resin–immiscible liquid interfaces.

Additionally, OCT imaging can be useful for capturing dynamics at resin interfaces and diagnosing problems such as deflection and relaxation. For example, in both cases of Fig. 8 *A*/*B*, taken after a 1 mm part was printed, the interface shows a net deflection downward past the point of its initial flat equilibrium position at the beginning of the print. This deflection is attributed to suboptimal print parameters which allow insufficient time after the return stroke of the pumped motion for the resin to relax to the intended slice thickness, exacerbated by the low restoring force provided by the liquid–liquid interface.

Proposing Novel VP Interfaces. To avoid these interfacial separation forces entirely, top–down VP methods do not require a window (76). However, these set-ups require a tank larger than the to-be-printed part and can still require significant support structures (77). VAM avoids separation forces entirely, allowing it to process highly viscous resins (14). However, without a build platform, challenges arise in ensuring cured polymer remains in the desired location without sinking, though printing in zero-gravity environments promises to alleviate this potential issue (78).

Toward Better VP Materials

From the outset, VP has relied on the use of photoinitiated curing reactions, typically making use of acrylate monomers. For example, in 1981, Kodama used a commercial resin known as "Tevista," which contained an acrylic ester cross-linker (19). Acrylates have enabled VP techniques over the past 40 y, but these materials tend to be brittle due to defects associated with the chain-growth polymerization mechanism and also have poor solvent resistance (79). The following sections describe advances in resin design that have enabled higher-functionality VP materials such as impact- and solvent-resistant plastics, flexible elastomers, polymer-derived organic materials, and multimaterials.

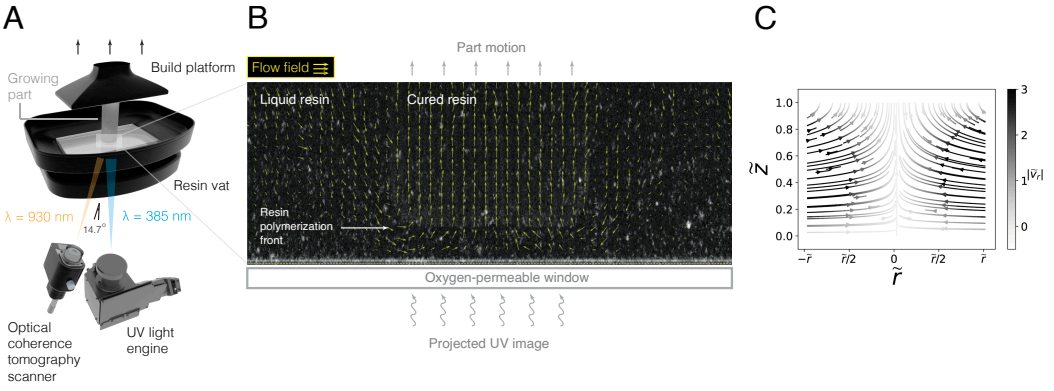

Fig. 7. OCT enables in situ observation of resin dynamics. (*A*) Schematic of OCT measurement during printing. The OCT scanner and UV light source converge at a spot in the resin bath where polymerization occurs. (*B*) A representative OCT image during printing of a cylinder. Image analysis enables flow fields to be ascertained. (*C*) Analytical solution of flow fields in the dead zone using the lubrication theory approximation, where $\tilde{z}$ and $\tilde{r}$ are vertical and radial position in dead zone, respectively, and $|\tilde{v}_r|$ is radial velocity.

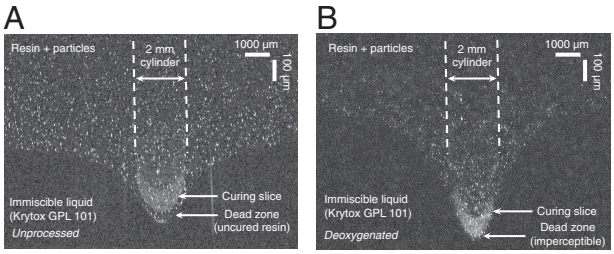

Fig. 8. OCT imaging of liquid window interface. Images of (*A*) a part printed above a resin–immiscible liquid and (*B*) the same process when the immiscible liquid has been degassed.

Photopolymer Advances. Extensive work has gone into developing photopolymer systems from prototyping resins to usage in structural applications with modest load-bearing components. Acrylate-based resins that undergo radical photopolymerization are commonly used due to their fast cure kinetics (30). These resins typically contain a mixture of multifunctional monomers (crosslinkers) and monofunctional monomers (reactive diluents). Increasing monomer functionality tends to increase network crosslink density, leading to stiff but brittle materials (80).

Challenges associated with acrylate systems include the fact that multifunctional monomers demonstrate gelation and autoacceleration early in the chain growth phase due to mobility hindrance of termination reactions, which are bimolecular in polymeric radical species (31). This leads to high kinetic chain lengths at early stages of polymerization, resulting in highly heterogeneous polymer networks. As the network gels, mobility of growing radical chains is restricted (81), typically leading to incomplete conversion of monomers and radicals. Finally, volumetric shrinkage occurs due to reduction in free volume during polymerization (82).

Approaches to improve material properties of acrylate networks include adding cycloaliphatic and aromatic acrylates to reduce the negative volume of reaction (83). Inclusion of less reactive methacrylate functional groups instead of acrylate functional groups has been favored due to the reduced toxicity of methacrylates (80). Variations in side chain length, functionality, and tacticity can influence glass transition temperature of the cured polymer system (84). Additionally, use of modified acrylates that exhibit hydrogen bonding such as urethane acrylates has been shown to improve curing kinetics and resulting mechanical properties relative to acrylates that do not experience hydrogen bonding (85). Finally, the addition of chain transfer agents can introduce step-growth behavior, leading to more uniform polymerized networks (80). In commercial systems, a combination of these strategies is needed to tune and optimize the properties of acrylate-based 3D printing resins.

Thiol-ene/yne photocuring chemistry has also been a long-standing alternative to acrylate radical polymerization (86). Thiol-based curing chemistry follows step-growth curing kinetics, enabling more uniform crosslink densities and higher double bond conversion relative to acrylate radical polymerization (87). However, poor shelf stability resulting from oxidative disulfide bond formation and an unpleasant odor have prevented widespread implementation of thiol-based resins; recent development of additives and systems based on secondary rather than primary thiols have shown promise for improving shelf life and reducing odor (88).

Photocurable epoxies (or oxetanes) can also be used in photopatterning applications with cationic photoinitiators or photoacid generators that initiate ring-opening polymerization (80). Like in acrylate systems, high crosslink densities in epoxies are correlated with high stiffness and low toughness. To reduce the brittleness of epoxy networks, strategies such as inclusion of hyperbranched polyesters (89) have been employed.

Within a variety of polymer systems, the inclusion of fillers such as metal oxides, silicate glasses, and inorganic-organic hybrids has also been used as a strategy to improve printed material properties such as modulus and impact strength, particularly in filled resins for dental applications (90). The inclusion of inorganic particles within the polymer matrix can yield improved properties via several mechanisms, including adhesion between particles and polymers, chain confinement effects, and shifting of brittle-ductile transition temperatures (80).

Beyond Polymers: Inorganic Materials and Composites. While VP was initially designed to fabricate polymeric structures, novel synthetic techniques have enabled printing of a variety of inorganic materials and composites (91, 92). These approaches still define the shape of a 3D printed part via selective curing of a photopolymer; inorganic precursors are included in the resin or introduced after printing. This approach has led to wide variety of new VP materials such as ceramics (93), glasses (94), carbon materials (95, 96), and metals (97, 98), shown in Fig. 9. Typically, precursors are incorporated as a suspension (97), as a homogeneous inorganic-organic mixture (99), dissolved in an aqueous resin (100), or infused into a gel

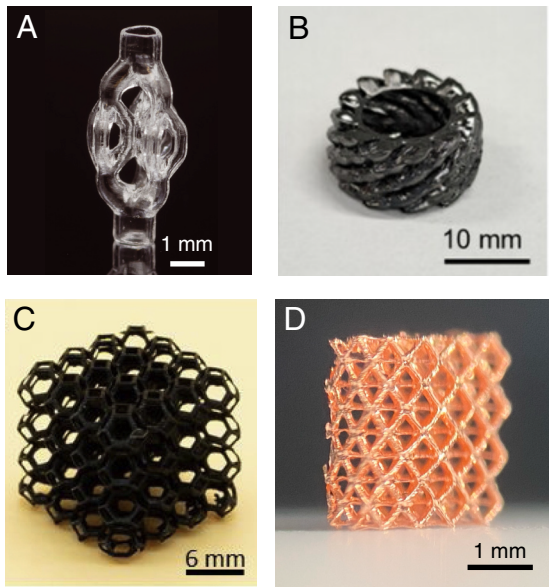

Fig. 9. Inorganic VP materials. (*A*) Glass fabricated with volumetric AM. Adapted with permission from ref. 102. (*B*) Pyrolytic carbon fabricated via projection-based VP. Adapted with permission from ref. 97. (*C*) Silicon oxycarbide ceramic fabricated via projection stereolithography. Adapted with permission from ref. 103. (*D*) Copper metal fabricated via hydrogel infusion of gels produced using projection stereolithography (98, 103).

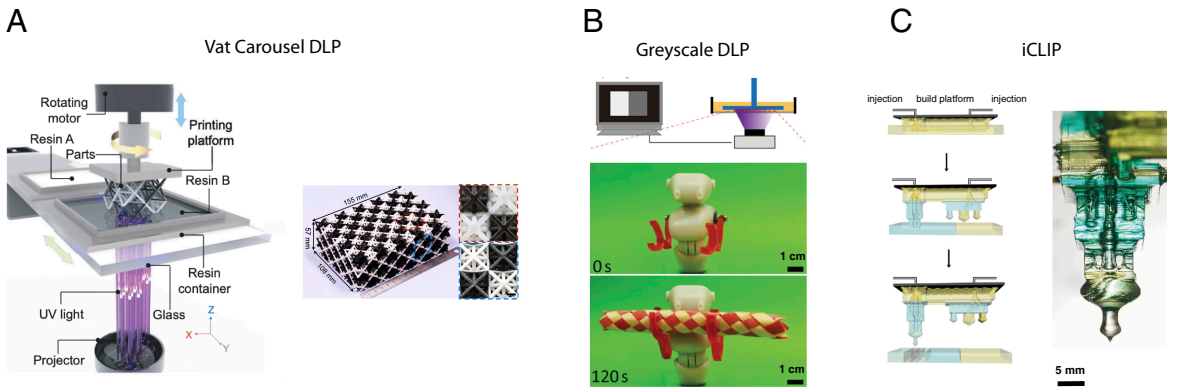

Fig. 10. Multimaterial VP techniques. (*A*) Vat carousel DLP, adapted from ref. 111, (*B*) Grayscale DLP, adapted from ref. 112, and (*C*) Injection CLIP, adapted from ref. 42.

after printing (98). These techniques broaden the scope of VP AM, enabling a wider range of functional materials to be fabricated with high-resolution and throughput and convenient processing conditions.

Doing More with Photopolymers: Dual-Cure Resins. In order to access a broader range of materials using photocurable systems, recent research has focused on the development of "dual cure" resins that incorporate two or more orthogonal polymerization chemistries. Typically, a first component composed of a photocurable resin is polymerized via a photoinitiated chain-growth process during 3D printing. The resulting gel structure is referred to as the "green state," and contains a secondary uncured resin component. Typically, this second component is thermally cured after completion of 3D printing (and also after solvent washing or mechanical cleaning to remove excess resin). The resulting interpenetrating polymer network can have improved material properties, chemical resistance, and printability compared to typical photocurable resins.

A common and commercially relevant example is the acrylate/epoxy dual cure resin system (104, 105). Photoinitiated radical polymerization of acrylate monomers is used to define part shape in a fast, oxygen-inhibited process, and subsequent step-growth polymerization of epoxides with nucleophilic diamines gives rise to enhanced material properties. For example, Carbon EPX 81 resin cure chemistry is shown in *SI Appendix*, Fig. S1. Other common dual-cure chemistries with first-stage UV-curable acrylate monomers include Michael-type additions, such as thiol-Michael or aza-Michael additions, which take advantage of the activated double bond in an acrylate group to add thiols or amines, respectively (106). Other common second-stage monomer systems include polyurethanes, polyurea/urethanes, cyanate esters, and silicones. Other types of postprocessing, such as reactive extraction, have also been used to create stretchable, elastomeric materials such as reinforced styrene-butadiene elastomers (107). In real-world product applications, such elastomeric materials can be used for highly deformable and reconfigurable designs (108, 109).

Multimaterials. 3D printing with multiple materials has numerous potential applications in areas such as functionally graded materials (112). This approach is established for extrusion (113) and direct ink write (114) approaches, which have achieved high precision multimaterial structures, albeit at relatively slow print speeds and with significant anisotropy. However, multimaterial VP has seen less rapid progress. This is largely due to the significant challenges associated with controlling fluid flows of multiple materials during VP. Nonetheless, several innovative approaches are summarized in Fig. 10.

Hardware-focused approaches to multimaterial VP typically employ vat-switching methods using, e.g., rotating carousels (115–117) or air jetting of multiple solution puddles (118), with researchers showing centrifugation can dramatically improve the resolution of these methods (110). Other materials-centric methods include formulating resins with varying monomer-cross linker ratios (119), orienting magnetic fillers anisotropically with external magnetic fields (120), using dual-cure resins cured partially by UV during printing and partially thermally afterward (121), or with multiwavelength UV projections (122). Others have sought to more tightly control the fluid dynamics at play within the vat during printing to achieve spatial gradients, such as with dynamic fluidic control (123) or by injecting resin spatioselectively into the vat through channels designed within the part itself (42). It remains a grand challenge to develop a high-throughput, high-resolution multimaterial VP printing platform.

Conclusion

In four decades, VP has been transformed from a novelty to a prototyping technique, to a rapidly industrializing process. Greater understanding of how light can grow materials at interfaces has led to marked advances in speed, resolution, and material properties of 3D-printed resins. The most impactful developments in this field have changed the way we think about these key factors; from the reimagining of photomasks as dynamic rather than static, the reinvention of interfaces that improve mass transport, and material synthesis schemes that enable fabrication of materials ranging from tough plastics to elastomers to metals. In the next decade, this field will push further into the mainstream of research and manufacturing, driven by key breakthroughs that continue to speed up VP while

maintaining high resolution, expand the palette of materials compatible with VP, and demonstrate mastery of free-form multimaterial printing.

Materials and Methods

OCT Imaging. OCT images were taken through transparent windows at the bottom of VP printers. The OCT system was placed approximately 15 degrees off-axis from the axis of UV illumination to prevent obscuring the UV light. The photopolymer resin is optically transparent at OCT operating wavelength of 930 nm; the resin contains 300 nm diameter TiO_2 particles which serve as contrast agents to help visualize the flow field and enable particle image velocimetry (PIV) analysis. Resin curing can be visualized with OCT due to increased backscattering of cured resin, which creates contrast between the cured part and the liquid resin. The cure front appears slightly lighter compared to uncured resin.

Rigid window OCT measurements. OCT images were taken through a transparent, oxygen-permeable, rigid window placed at the bottom of a vat polymerization printer. OCT image frames were taken through the vertical midplane of a 2 mm wide by 25 mm deep part during printing under continuous draw with a velocity of 40 mm per hour. Parts were printed using Carbon PR3 XG resin (E_c = 10.9 mJ/cm^2, D_p = 108 μm) with a UV intensity of 2.0 mW/cm^2. During printing, an atmosphere of 100% O_2 at atmospheric pressure was present beneath the window. The flow field was extracted using Matlab's PIV Lab (124).

Liquid window OCT measurements. Similar OCT images were taken while printing above a liquid window of GLP101 Fluorinert (density: 1.9 g/mL; viscosity: 32 cP) which had been equilibrated with an air atmosphere at room temperature. The liquid thickness was 5.0 mm, and the liquid was static during printing. Parts were printed with Carbon PR Clear urethane acrylate resin (E_c = 23 mJ/cm^2, D_p = 1,500 μm; viscosity: 1,650 cP) at a UV intensity of approximately 4 mW/cm^2. In pumped mode, the pump height was 2.5 mm. The estimated dead zone thickness based on OCT observations was 30 to 40 μm.

Data, Materials, and Software Availability. All study data are included in the article and/or supporting information. Previously published data were used for this work. Previously published data is used to create Table 1, with citations given in the manuscript (15, 18, 22, 42, 43, 45–48).

ACKNOWLEDGMENTS. This work was supported by the Precourt Institute for Energy at Stanford, the Wu Tsai Human Performance Alliance at Stanford, the Bill and Melinda Gates Foundation (No. INV046940), the Wellcome Leap R3 Program, and the NIH. Carbon provided the materials used in optical coherence tomography experiments. K.H. was supported by the Wu Tsai Human Performance Alliance Postdoctoral Fellowship. G.L. and J.M.K. were supported by the NSF Graduate Research Fellowship Program under Grant No. DGE-1656518. Any opinions, findings, and conclusions or recommendations expressed in this material are those of the authors and do not necessarily reflect the views of the NSF.

1. M. Pagac *et al*., A review of vat photopolymerization technology: Materials, applications, challenges, and future trends of 3D printing. *Polymers* **13**, 1–20 (2021).
2. J. A. Lewis, Direct ink writing of 3D functional materials. *Adv. Funct. Mater.* **16**, 2193–2204 (2006).
3. M. Ziaee, N. B. Crane, Binder jetting: A review of process, materials, and methods. *Addit. Manuf.* **28**, 781–801 (2019).
4. W. E. King *et al*., Laser powder bed fusion additive manufacturing of metals: Physics, computational, and materials challenges. *Appl. Phys. Rev.* **2**, 041304 (2015).
5. J. Panetta *et al*., Elastic textures for additive fabrication. *ACM Trans. Graphics* **34**, 1–12 (2015).
6. J. Martínez, J. Dumas, S. Lefebvre, Procedural voronoi foams for additive manufacturing. *ACM Trans. Graphics* **35**, 1–12 (2016).
7. J. Martínez, S. Hornus, H. Song, S. Lefebvre, Polyhedral voronoi diagrams for additive manufacturing. *ACM Trans. Graphics* **37**, 1–15 (2018).
8. H. K. Dave, R. T. Karumuri, A. R. Prajapati, S. R. Rajpurohit, Specific energy absorption during compression testing of ABS and FPU parts fabricated using LCD–SLA based 3D printer. *Rapid Prototyping J.* **28**, 1530–1540 (2022).
9. Z. J. Patterson, D. K. Patel, S. Bergbreiter, L. Yao, C. Majidi, A method for 3D printing and rapid prototyping of fieldable untethered soft robots. *Soft Robot.* **10**, 292–300 (2023).
10. M. V. Varma, B. Kandasubramanian, S. M. Ibrahim, 3D printed scaffolds for biomedical applications. *Mater. Chem. Phys.* **255**, 123642 (2020).
11. V. Harinarayana, Y. Shin, Two-photon lithography for three-dimensional fabrication in micro/nanoscale regime: A comprehensive review. *Opt. Laser Technol.* **142**, 107180 (2021).
12. W. Haske *et al*., 65 nm feature sizes using visible wavelength 3-D multiphoton lithography. *Opt. Express* **15**, 3426 (2007).
13. Z. Gan, Y. Cao, R. A. Evans, M. Gu, Three-dimensional deep sub-diffraction optical beam lithography with 9 nm feature size. *Nat. Commun.* **4**, 2061 (2013).
14. B. E. Kelly *et al*., Volumetric additive manufacturing via tomographic reconstruction. *Science* **363**, 1075–1079 (2019).
15. J. R. Tumbleston *et al*., Continuous liquid interface production of 3D objects. *Science* **347**, 1349–1352 (2015).
16. M. P. De Beer *et al*., Rapid, continuous additive manufacturing by volumetric polymerization inhibition patterning. *Sci. Adv.* **5**, eaau8723 (2019).
17. D. Loterie, P. Delrot, C. Moser, High-resolution tomographic volumetric additive manufacturing. *Nat. Commun.* **11**, 852 (2020).
18. M. Regehly *et al*., Xolography for linear volumetric 3D printing. *Nature* **588**, 620–624 (2020).
19. H. Kodama, Automatic method for fabricating a three-dimensional plastic model with photo-hardening polymer. *Rev. Sci. Inst.* **52**, 1770–1773 (1981).
20. C. W. Hull, Apparatus for production of three-dimensional objects by stereolithography (1986). U.S. Patent No. 4,575,330.
21. A. Bertsch, J. Jézéquel, J. André, Study of the spatial resolution of a new 3D microfabrication process: The microstereophotolithography using a dynamic mask-generator technique. *J. Photochem. Photobiol. A: Chem.* **107**, 275–281 (1997).
22. C. Sun, N. Fang, D. Wu, X. Zhang, Projection micro-stereolithography using digital micro-mirror dynamic mask. *Sens. Actuators A: Phys.* **121**, 113–120 (2005).
23. A. K. O'Brien, C. N. Bowman, Impact of oxygen on photopolymerization kinetics and polymer structure. *Macromolecules* **39**, 2501–2506 (2006).
24. R. G. Norrish, C. H. Bamford, Photo-decomposition of aldehydes and ketones. *Nature* **140**, 195–196 (1937).
25. Y. Bao, Recent trends in advanced photoinitiators for VAT photopolymerization 3D printing. *Macromol. Rapid Commun.* **43**, 1–15 (2022).
26. A. Bagheri, J. Jin, Photopolymerization in 3D printing. *ACS Appl. Polym. Mater.* **1**, 593–611 (2019).
27. D. Ahn, L. M. Stevens, K. Zhou, Z. A. Page, Rapid high-resolution visible light 3D printing. *ACS Central Sci.* **6**, 1555–1563 (2020).
28. J. Zhou, X. Allonas, A. Ibrahim, X. Liu, Progress in the development of polymeric and multifunctional photoinitiators. *Progr. Polym. Sci.* **99**, 101165 (2019).
29. C. Barner-Kowollik, Acrylate free radical polymerization: From mechanism to polymer design. *Macromol. Rapid Commun.* **30**, 1961–1963 (2009).
30. A. M. van Herk, Historic account of the development in the understanding of the propagation kinetics of acrylate radical polymerizations. *Macromol. Rapid Commun.* **30**, 1964–1968 (2009).
31. T. M. Lovestead, J. A. Burdick, K. S. Anseth, C. N. Bowman, Understanding multivinyl monomer photopolymerization kinetics through modeling and GPC investigation of degradable networks. *Polymer* **46**, 6226–6234 (2005).
32. H. Stutz, K. H. Illers, J. Mertes, A generalized theory for the glass transition temperature of crosslinked and uncrosslinked polymers. *J. Polym. Sci., Part B: Polym. Phys.* **28**, 1483–1498 (1990).
33. G. I. Peterson *et al*., Production of materials with spatially-controlled cross-link density via VAT photopolymerization. *ACS Appl. Mater. Interfaces* **8**, 29037–29043 (2016).
34. P. F. Jacobs, *Fundamentals of Stereolithography* (Society of Manufacturing Engineers, 1992), pp. 196–211.
35. M. L. Griffith, J. W. Halloran, Scattering of ultraviolet radiation in turbid suspensions. *J. Appl. Phys.* **81**, 2538–2546 (1997).
36. Z. D. Pritchard, M. P. Beer, R. J. Whelan, T. F. Scott, M. A. Burns, Modeling and correcting cure-through in continuous stereolithographic 3D printing. *Adv. Mater. Technol.* **4**, 1900700 (2019).
37. J. L. Sanchez Noriega *et al*., Spatially and optically tailored 3D printing for highly miniaturized and integrated microfluidics. *Nat. Commun.* **12**, 5509 (2021).
38. J. Bennett, Measuring UV curing parameters of commercial photopolymers used in additive manufacturing. *Addit. Manuf.* **18**, 203–212 (2017).
39. B. Grigoryan *et al*., Multivascular networks and functional intravascular topologies within biocompatible hydrogels. *Science* **364**, 458–464 (2019).
40. H. Gong, M. Beauchamp, S. Perry, A. T. Woolley, G. P. Nordin, Optical approach to resin formulation for 3D printed microfluidics. *RSC Adv.* **5**, 106621–106632 (2015).
41. Y. Xu *et al*., In-situ transfer vat photopolymerization for transparent microfluidic device fabrication. *Nat. Commun.* **13**, 918 (2022).
42. G. Lipkowitz *et al*., Injection continuous liquid interface production of 3D objects. *Sci. Adv.* **8**, eabq3917 (2022).
43. D. A. Walker, J. L. Hedrick, C. A. Mirkin, Rapid, large-volume, thermally controlled 3D printing using a mobile liquid interface. *Science* **366**, 360–364 (2019).
44. A. Dobos *et al*., Thiol-gelatin-norbornene bioink for laser-based high-definition bioprinting. *Adv. Health Mater.* **9**, 1900752 (2020).
45. S. K. Saha *et al*., Scalable submicrometer additive manufacturing. *Science* **366**, 105–109 (2019).
46. M. Shusteff *et al*., One-step volumetric additive manufacturing of complex polymer structures. *Sci. Adv.* **3**, eaao5496 (2017).
47. A. Orth *et al*., Deconvolution volumetric additive manufacturing. *Nat. Commun.* **14**, 4412 (2023).

48. K. Kowsari, S. Akbari, D. Wang, N. X. Fang, Q. Ge, High-efficiency high-resolution multimaterial fabrication for digital light processing-based three-dimensional printing. *3D Printing Addit. Manuf.* **5**, 185–193 (2018).
49. K. Hsiao *et al*., Single-digit-micrometer-resolution continuous liquid interface production. *Sci. Adv.* **8**, eabq2846 (2022).
50. Y. Pan, H. He, J. Xu, A. Feinerman, Study of separation force in constrained surface projection stereolithography. *Rapid Prototyping J.* **23**, 353–361 (2017).
51. Y. M. Huang, C. P. Jiang, On-line force monitoring of platform ascending rapid prototyping system. *J. Mater. Process. Technol.* **159**, 257–264 (2005).
52. F. D. Frumosu, M. Méndez Ribó, S. Shan, Y. Zhang, M. Kulahci, Online monitoring for error detection in VAT photopolymerization. *Int. J. Comput. Integr. Manuf.* **36**, 1313–1330 (2023).
53. A. Khadilkar, J. Wang, R. Rai, Deep learning-based stress prediction for bottom-up SLA 3D printing process. *Int. J. Adv. Manuf. Technol.* **102**, 2555–2569 (2019).
54. K. Zhu, A. Dancu, S. Zhao, "Fuseprint: A diy 2.5 d printing technique for good-fit fabrication with daily objects" in *Proceedings of the 2017 CHI Conference Extended Abstracts on Human Factors in Computing Systems* (2017), pp. 413–416.
55. K. Kowsari *et al*., Photopolymer formulation to minimize feature size, surface roughness, and stair-stepping in digital light processing-based three-dimensional printing. *Addit. Manuf.* **24**, 627–638 (2018).
56. J. Jin, J. Yang, H. Mao, Y. Chen, A vibration-assisted method to reduce separation force for stereolithography. *J. Manuf. Process.* **34**, 793–801 (2018).
57. X. Li, H. Mao, Y. Pan, Y. Chen, Mask video projection-based stereolithography with continuous resin flow. *J. Manuf. Sci. Eng.* **141**, 081007 (2019).
58. H. Song *et al*., Development of a variable tensioning system to reduce separation force in large scale stereolithography. *Addit. Manuf.* **38**, 101816 (2021).
59. J. C. Wang, M. Ruilova, Y. H. Lin, The development of an active separation method for bottom-up stereolithography system (IEEE/SICE International Symposium on System Integration, 2017), pp. 108–114.
60. D. Dendukuri *et al*., Modeling of oxygen-inhibited free radical photopolymerization in a PDMS microfluidic device. *Macromolecules* **41**, 8547–8556 (2008).
61. R. Janusziewicz, J. R. Tumbleston, A. L. Quintanilla, S. J. Mecham, J. M. DeSimone, Layerless fabrication with continuous liquid interface production. *Proc. Natl. Acad. Sci. U.S.A.* **113**, 11703–11708 (2016).
62. Y. Jiang *et al*., Textured window design for continuous projection stereolithography process. *Manuf. Lett.* **24**, 87–91 (2020).
63. H. He, Y. Pan, A. Feinerman, J. Xu, Air-diffusion-channel constrained surface based stereolithography for three-dimensional printing of objects with wide solid cross sections. *J. Manuf. Sci. Eng.* **140**, 061011 (2018).
64. A. Lamberti, S. Marasso, M. Cocuzza, PDMS membranes with tunable gas permeability for microfluidic applications. *RSC Adv.* **4**, 61415–61419 (2014).
65. F. Liravi, S. Das, C. Zhou, Separation force analysis and prediction based on cohesive element model for constrained-surface stereolithography processes. *Comput.-Aided Des.* **69**, 134–142 (2015).
66. D. Gritsenko *et al*., On characterization of separation force for resin replenishment enhancement in 3D printing. *Addit. Manuf.* **17**, 151–156 (2017).
67. Y. Pan, C. Zhou, Y. Chen, J. Partanen, Multitool and multi-axis computer numerically controlled accumulation for fabricating conformal features on curved surfaces. *J. Manuf. Sci. Eng.* **136**, 031007 (2014).
68. S. Aumann, S. Donner, J. Fischer, F. Müller, "Optical coherence tomography (OCT): Principle and technical realization" in *High Resolution Imaging in Microscopy and Ophthalmology: New Frontiers in Biomedical Optics* (Springer, 2019), pp. 59–85.
69. D. P. Popescu *et al*., Optical coherence tomography: Fundamental principles, instrumental designs and biomedical applications. *Biophys. Rev.* **3**, 155–169 (2011).
70. A. Al-Mujaini, U. K. Wali, S. Azeem, Optical coherence tomography: Clinical applications in medical practice. *Oman Med. J.* **28**, 86 (2013).
71. Y. Wang *et al*., Application of optical coherence tomography in clinical diagnosis. *J. X-ray Sci. Technol.* **27**, 995–1006 (2019).
72. J. G. Fujimoto, C. Pitris, S. A. Boppart, M. E. Brezinski, Optical coherence tomography: An emerging technology for biomedical imaging and optical biopsy. *Neoplasia* **2**, 9–25 (2000).
73. A. Davis, S. Boppart, F. Rothenberg, J. Izatt, "OCT applications in developmental biology" in *Optical Coherence Tomography. Biological and Medical Physics, Biomedical Engineering* (Springer, 2008), pp. 919–959.
74. M. Everett, S. Magazzeni, T. Schmoll, M. Kempe, Optical coherence tomography: From technology to applications in ophthalmology. *Transl. Biophotons* **3**, e202000012 (2021).
75. E. P. Wesseler, R. Iltis, L. C. Clark Jr, The solubility of oxygen in highly fluorinated liquids. *J. Fluorine Chem.* **9**, 137–146 (1977).
76. V. Chan, P. Zorlutuna, J. H. Jeong, H. Kong, R. Bashir, Three-dimensional photopatterning of hydrogels using stereolithography for long-term cell encapsulation. *Lab Chip* **10**, 2062–2070 (2010).
77. N. Mulka, T. Goyal, A. Jariwala, D. Rosen, "Static liquid interface to reduce support structure necessity in top-down stereolithography" in *2021 International Solid Freeform Fabrication Symposium* (University of Texas at Austin, 2021).
78. T. Waddell *et al*., Use of volumetric additive manufacturing as an in-space manufacturing technology. *Acta Astronaut.* **211**, 474–482 (2023).
79. J. J. Schwartz, Additive manufacturing: Frameworks for chemical understanding and advancement in VAT photopolymerization. *MRS Bull.* **47**, 628–641 (2022).
80. S. C. Ligon-Auer, M. Schwentenwein, C. Gorsche, J. Stampfl, R. Liska, Toughening of photo-curable polymer networks: A review. *Polym. Chem.* **7**, 257–286 (2016).
81. M. D. Goodner, C. N. Bowman, Development of a comprehensive free radical photopolymerization model incorporating heat and mass transfer effects in thick films. *Chem. Eng. Sci.* **57**, 887–900 (2002).
82. K. S. Anseth, C. M. Wang, C. N. Bowman, Reaction behaviour and kinetic constants for photopolymerizations of multi(meth)acrylate monomers. *Polymer* **35**, 3243–3250 (1994).
83. L. U. Kim, J. W. Kim, C. K. Kim, Effects of molecular structure of the resins on the volumetric shrinkage and the mechanical strength of dental restorative composites. *Biomacromolecules* **7**, 2680–2687 (2006).
84. T. Li *et al*., Chain flexibility and glass transition temperatures of poly(n-alkyl (meth)acrylate)s: Implications of tacticity and chain dynamics. *Polymer* **213**, 123207 (2021).
85. H. Bakhshi, G. Kuang, F. Wieland, W. Meyer, Photo-curing kinetics of 3D-printing photo-inks based on urethane–acrylates. *Polymers* **14**, 2974 (2022).
86. C. R. Morgan, F. Magnotta, A. D. Ketley, Thiol/ene photocurable polymers. *J. Polym. Sci. Polym. Chem. Ed.* **15**, 627–645 (1977).
87. C. E. Hoyle, C. N. Bowman, Thiol-ene click chemistry. *Angew. Chem. Int. Ed.* **49**, 1540–1573 (2010).
88. L. Chen, Q. Wu, G. Wei, R. Liu, Z. Li, Highly stable thiol-ene systems: From their structure-property relationship to DLP 3D printing. *J. Mater. Chem. C* **6**, 11561–11568 (2018).
89. D. Foix, A. Serra, L. Amparore, M. Sangermano, Impact resistance enhancement by adding epoxy ended hyperbranched polyester to DGEBA photocured thermosets. *Polymer* **53**, 3084–3088 (2012).
90. E. Habib, R. Wang, Y. Wang, M. Zhu, X. X. Zhu, Inorganic fillers for dental resin composites: Present and future. *ACS Biomater. Sci. Eng.* **2**, 1–11 (2016).
91. M. Layani, X. Wang, S. Magdassi, Novel materials for 3D printing by photopolymerization. *Adv. Mater.* **30**, 1–7 (2018).
92. D. W. Yee, J. R. Greer, Three–dimensional chemical reactors: *In situ* materials synthesis to advance VAT photopolymerization. *Polym. Int.* **70**, 964–976 (2021).
93. Z. Chen *et al*., 3D printing of ceramics: A review. *J. Eur. Ceram. Soc.* **39**, 661–687 (2019).
94. D. Zhang, X. Liu, J. Qiu, 3D printing of glass by additive manufacturing techniques: A review. *Front. Optoelectron.* **14**, 263–277 (2020).
95. J. Bauer, A. Schroer, R. Schwaiger, O. Kraft, Approaching theoretical strength in glassy carbon nanolattices. *Nat. Mater.* **15**, 438–443 (2016).
96. V. A. Bobrin *et al*., Design and 3D printing of polyacrylonitrile-derived nanostructured carbon architectures. *Small Sci.* **4**, 2300275 (2024).
97. H. X. Nguyen, H. Suen, B. Poudel, P. Kwon, H. Chung, Development of an innovative, high speed, large-scaled, and affordable metal additive manufacturing process. *CIRP Ann.* **69**, 177–180 (2020).
98. M. A. Saccone, R. A. Gallivan, K. Narita, D. W. Yee, J. R. Greer, Additive manufacturing of micro-architected metals via hydrogel infusion. *Nature* **612**, 685–690 (2022).
99. A. Vyatskikh, A. Kudo, S. Delalande, J. R. Greer, Additive manufacturing of polymer-derived titania for one-step solar water purification. *Mater. Today Commun.* **15**, 288–293 (2018).
100. D. W. Yee *et al*., Hydrogel-based additive manufacturing of lithium cobalt oxide. *Adv. Mater. Technol.* **6**, 2000791 (2021).
101. J. T. Toombs *et al*., Volumetric additive manufacturing of silica glass with microscale computed axial lithography. *Science* **376**, 308–312 (2022).
102. X. Wang *et al*., Additive manufacturing of ceramics from preceramic polymers: A versatile stereolithographic approach assisted by thiol-ene click chemistry. *Addit. Manuf.* **27**, 80–90 (2019).
103. M. Eisenstein, Seven technologies to watch in 2024. *Nature* **625**, 844–848 (2024).
104. C. Decker, T. Nguyen Thi Viet, D. Decker, E. Weber-Koehl, UV-radiation curing of acrylate/epoxide systems. *Polymer* **42**, 5531–5541 (2001).
105. J. Cushen, J. Goodrich, J. P. Rolland, Epoxy dual cure resins for additive manufacturing (2017). Patent No. WO2017044381A1.
106. O. Konuray, X. Fernández-Francos, X. Ramis, A. Serra, State of the art in dual-curing acrylate systems. *Polymers* **10**, 178 (2018).
107. C. Kasprzak *et al*., VAT photopolymerization of reinforced styrene-butadiene elastomers: A degradable scaffold approach. *ACS Appl. Mater. Interfaces* **14**, 18965–18973 (2022).
108. Z. Yan, H. Peng, "FabHydro: Printing interactive hydraulic devices with an affordable SLA 3D printer" in *The 34th Annual ACM Symposium on User Interface Software and Technology* (2021), pp. 298–311.
109. Z. Zhakypov, A. M. Okamura, "Fingerprint: A 3-D printed soft monolithic 4-degree-of-freedom fingertip haptic device with embedded actuation" in *2022 IEEE 5th International Conference on Soft Robotics (RoboSoft)* (IEEE, 2022), pp. 938–944.
110. J. Cheng *et al*., Centrifugal multimaterial 3D printing of multifunctional heterogeneous objects. *Nat. Commun.* **13**, 7931 (2022).
111. X. Kuang *et al*., Grayscale digital light processing 3D printing for highly functionally graded materials. *Sci. Adv.* **5**, eaav5790 (2019).
112. J. Mueller, K. Shea, Stepwise graded struts for maximizing energy absorption in lattices. *Extreme Mech. Lett.* **25**, 7–15 (2018).
113. D. Yadav, D. Chhabra, R. K. Garg, A. Ahlawat, A. Phogat, Optimization of FDM 3D printing process parameters for multi-material using artificial neural network. *Mater. Today: Proc.* **21**, 1583–1591 (2020).
114. M. A. Skylar-Scott, J. Mueller, C. W. Visser, J. A. Lewis, Voxelated soft matter via multimaterial multinozzle 3D printing. *Nature* **575**, 330–335 (2019).
115. H. T. Maia, D. Li, Y. Yang, C. Zheng, LayerCode: Optical barcodes for 3D printed shapes. *ACM Trans. Graphics* **38**, 1–14 (2019).
116. B. Khatri, M. Frey, A. Raouf-Fahmy, M. V. Scharla, T. Hanemann, Development of a multi-material stereolithography 3D printing device. *Micromachines* **11**, 532 (2020).
117. C. Zhou, Y. Chen, Z. Yang, B. Khoshnevis, "Development of a multi-material mask-image-projection-based stereolithography for the fabrication of digital materials" in *2011 International Solid Freeform Fabrication Symposium* (University of Texas at Austin, 2011).
118. Q. Ge *et al*., 3D printing of highly stretchable hydrogel with diverse UV curable polymers. *Sci. Adv.* **7**, eaba4261 (2021).
119. J. Borrello, P. Nasser, J. C. Iatridis, K. D. Costa, 3D printing a mechanically-tunable acrylate resin on a commercial DLP-SLA printer. *Addit. Manuf.* **23**, 374–380 (2018).
120. H. Younes *et al*., Magnetic-field-assisted DLP stereolithography for controlled production of highly aligned 3D printed polymer-Fe_3O_4@ graphene nanocomposites. *Mater. Res. Bull.* **154**, 111938 (2022).
121. J. Bachmann *et al*., Cavity VAT photopolymerisation for additive manufacturing of polymer-composite 3D objects. *Commun. Mater.* **2**, 1–9 (2021).
122. J. Schwartz, A. Boydston, Multimaterial actinic spatial control 3D and 4D printing. *Nat. Commun.* **10**, 1–10 (2019).
123. D. Han, C. Yang, N. X. Fang, H. Lee, Rapid multi-material 3D printing with projection micro-stereolithography using dynamic fluidic control. *Addit. Manuf.* **27**, 606–615 (2019).
124. W. Thielicke, R. Sonntag, Particle image velocimetry for MatLab: Accuracy and enhanced algorithms in PIVlab. *J. Open Res. Software* **9**, 12 (2021).